

Dual-Site Mg/Zn Substitution in Fe–Mn–Ni Layered Oxides: High-Entropy Engineering for Stable Oxygen Redox and Enhanced Sodium-Ion Storage

Xiangpeng Kong, Fujun Niu,* Xing Yan, Qiang Rong, Junqiao Xiong, Zhengwei Li, Huai Chen, Liang Qiu, and Shaohua Shen*

The development of high-performance O₃-type cathode materials for sodium-ion batteries (SIBs) is hindered by structural instability and limited reversibility of oxygen redox reactions (ORR). Herein, a dual-substitution strategy is proposed to synergistically activate stable ORR and structural reinforcement in NaFe_{0.33}Mn_{0.33}Ni_{0.33}O₂ (FMN). Mg substitution induces anion redox activity, achieving a high initial capacity of 163.2 mAh g⁻¹, while Zn substitution stabilizes the host structure, enabling 71.6% capacity retention after 100 cycles. By integrating these effects through high-entropy engineering, NaMg_{0.1}Zn_{0.15}Fe_{0.11}Mn_{0.4}Ni_{0.23}O₂

(MZFMN) is synthesized, which exhibits a balanced electrochemical performance, with a high initial discharge capacity of 154.5 mAh g⁻¹ and superior cyclability of 78.0% retention after 100 cycles. Mechanistic studies reveal that Mg facilitates reversible ORR, Zn mitigates phase transitions via covalent Zn–O bonding, and the high-entropy configuration suppresses irreversible structural degradation. This work establishes a paradigm for designing multifunctional cathodes by combining cation substitution and entropy-driven stabilization, advancing SIBs toward practical energy storage applications.

1. Introduction

Sodium-ion batteries (SIBs) have emerged as a promising technology for large-scale energy storage applications due to their abundant resources, low costs, and environmental friendliness.^[1] However, their commercialization hinges on the development of cathode materials that concurrently deliver high energy density, long-term cyclability, and structural robustness.^[2] Among cathode candidates, O₃-type layered transition metal (TM) oxides (e.g., NaFe_{0.33}Mn_{0.33}Ni_{0.33}O₂, FMN) are particularly promising due to their high theoretical capacity and earth-abundant constituents. Yet, these materials suffer from rapid capacity decay caused by irreversible oxygen redox reactions (ORR) and detrimental phase transitions during cycling, which destabilize the host framework and exacerbate TM dissolution.^[3] To mitigate these limitations, it is essential to optimize the structure and properties

of cathode materials, thereby ensuring improved electrochemical performance and overall battery reliability.

Cation substitution has proven effective in modulating redox activity and structural dynamics.^[4] Specifically, the substitution of Mg and Zn ions has garnered significant attention due to their ability to inhibit unfavorable phase transitions and stabilize material structures. For instance, Mg²⁺ doping in layered oxides could activate anion redox to boost capacity, as demonstrated in P2-Na_{0.67}Ni_{0.3-x}Mg_xMn_{0.7}O₂, where Mg promoted ORR without oxygen release.^[5] Niu et al. demonstrated that Mg substitution in O₃-Na_{0.67}Mg_{0.28}Mn_{0.72}O₂ could not only enhance initial capacity but also enable ORR without oxygen release, further highlighting the potential benefits of cation substitution in SIB cathodes.^[6] Zn-substituted cathode materials have been shown to exhibit more reversible ORR with no significant O₂ release during cycling, leading to improved cycle stability. This enhanced performance is attributed to the higher electronegativity of Zn, which generates more covalent Zn–O bond, resulting in stronger binding of oxygen.^[7] For example, P2-Na_{2/3}Mn_{0.7}Zn_{0.3}O₂ could retain 80.0% of capacity even after 200 cycles within a voltage range of 1.5–4.6 V.^[8] Notwithstanding the benefits of monosubstitution strategies, these approaches often come with trade-offs, where Mg-rich systems may suffer from capacity fading due to irreversible oxygen loss, while Zn-dominated materials compromise specific capacity in pursuit of stability. This conflict highlights the need for a synergistic approach that effectively decouples capacity enhancement from structural degradation, thereby, enabling the development of high-performance electrodes that simultaneously exhibit superior capacity and durability.

In this study, we introduce a dual-substitution strategy, integrated with high-entropy engineering, to overcome the challenges faced by FMN cathodes in SIBs. By cosubstituting Mg and

X. Kong, Q. Rong, J. Xiong
Hunan Desay Battery Co. Ltd.
Changsha 410203, P. R. China

F. Niu, H. Chen, L. Qiu
School of Advanced Energy
Sun Yat-sen University (Shenzhen)
Shenzhen 518107, China
E-mail: niufujun@mail.sysu.edu.cn

X. Yan, Z. Li, S. Shen
International Research Center for Renewable Energy
State Key Laboratory of Multiphase Flow in Power Engineering
Xi'an Jiaotong University
Xi'an, Shaanxi 710049, China
E-mail: shshen_xjtu@mail.xjtu.edu.cn

 Supporting information for this article is available on the WWW under <https://doi.org/10.1002/batt.202500413>

Zn at distinct TM sites, we synthesized a high-entropy material, $\text{NaMg}_{0.1}\text{Zn}_{0.15}\text{Fe}_{0.11}\text{Mn}_{0.4}\text{Ni}_{0.23}\text{O}_2$ (MZFMN), and systematically elucidated how the synergy between Mg and Zn, as well as entropy stabilization, collectively enhanced sodium storage performance. Our results demonstrate that MZFMN achieves an exceptional initial discharge capacity of 154.5 mAh g^{-1} with a remarkable 78% capacity retention after 100 cycles, outperforming mono-substituted analogs. This high performance is attributed to the Mg promoted ORR activity, the phase-stabilization effect and facilitated sodium-ion transfer by Zn substitution, and the entropy-driven disorder suppressing irreversible structural rearrangements. By introducing a groundbreaking “dual-ion synergy and entropy stabilization” strategy that fundamentally advances O₃-type cathode design, this work establishes a paradigm for designing high-entropy cathodes that addresses traditional performance trade-offs, paving the way for practical SIB applications.

2. Results and Discussion

In this study, a series of Mg/Zn-substituted $\text{NaFe}_{0.33}\text{Mn}_{0.33}\text{Ni}_{0.33}\text{O}_2$ (FMN) layered oxide cathode materials, including Mg-substituted variants $\text{NaMg}_x\text{Fe}_{0.33}\text{Mn}_{0.33}\text{Ni}_{0.33-x}\text{O}_2$ (MFMN-x), Zn-substituted variants $\text{NaZn}_x\text{Fe}_y\text{Mn}_z\text{Ni}_{0.33}\text{O}_2$ (ZFMN-x; $x+y+z=0.66$), and Mg/Zn cosubstituted compound $\text{NaMg}_{0.1}\text{Zn}_{0.15}\text{Fe}_{0.11}\text{Mn}_{0.4}\text{Ni}_{0.23}\text{O}_2$ (MZFMN), were synthesized via a high-temperature solid-state method, with chemical formulas summarized in Table S1 in Supporting Information. The morphologies of pristine FMN, partially substituted MFMN-0.1 (as an example), and fully substituted MFMN-0.33 were initially examined using scanning electron microscopy (SEM). As shown in Figure 1a–c, all three samples exhibit the characteristic plate morphology of layered oxides,

featuring smooth surfaces and an average particle size of $\approx 1\text{--}2 \mu\text{m}$.^[9] Importantly, the substitution of Mg demonstrates minimal impact on the particle size distribution of FMN, suggesting that this modification may preserve the rheological properties of electrode slurries, and thus, maintain the electrochemical performance of the resulting batteries.^[10] Energy-dispersive spectroscopy (EDS) mapping confirms homogeneous spatial distribution of Na, Mg, Ni, Fe, Mn, and O in MFMN-0.1, verifying successful solid-state synthesis without elemental segregation (Figure S1, Supporting Information). Complementary transmission electron microscopy (TEM) analysis reveals well-defined sheet-like architectures with distinct dot matrix patterns in selected-area electron diffraction (SAED), confirming single-crystalline characteristics (Figure S2a,b, Supporting Information).^[11] Additionally, high-resolution TEM (HRTEM) imaging resolves hexagonal metal-ion arrangements, demonstrating both crystallographic order and transition-metal layer organization essential for charge transport dynamics (Figure S2c, Supporting Information).^[12]

The X-ray diffraction (XRD) patterns of FMN and MFMN-x, as shown in Figure 1d, display that the diffraction peaks of both materials closely match those of $\text{NaMn}_{0.5}\text{Ni}_{0.5}\text{O}_2$, confirming an O₃-type hexagonal structure (R3m space group) with no phase transitions during substitution.^[13] Notably, the (003) peak of MFMN-x shifts toward lower angles compared to that of pristine FMN, suggesting successful incorporation of Mg into the crystal lattice and expansion of the (003) interplanar spacing (Figure 1e).^[14] The Rietveld refinement pattern of MFMN-0.1 exhibits excellent agreement with the raw XRD data (Figure 1f), validating the structural model. Furthermore, the refined lattice parameters (Table S2, Supporting Information) reveal that the introduction of Mg could induce significant structural modifications of FMN material. Figure S3, Supporting

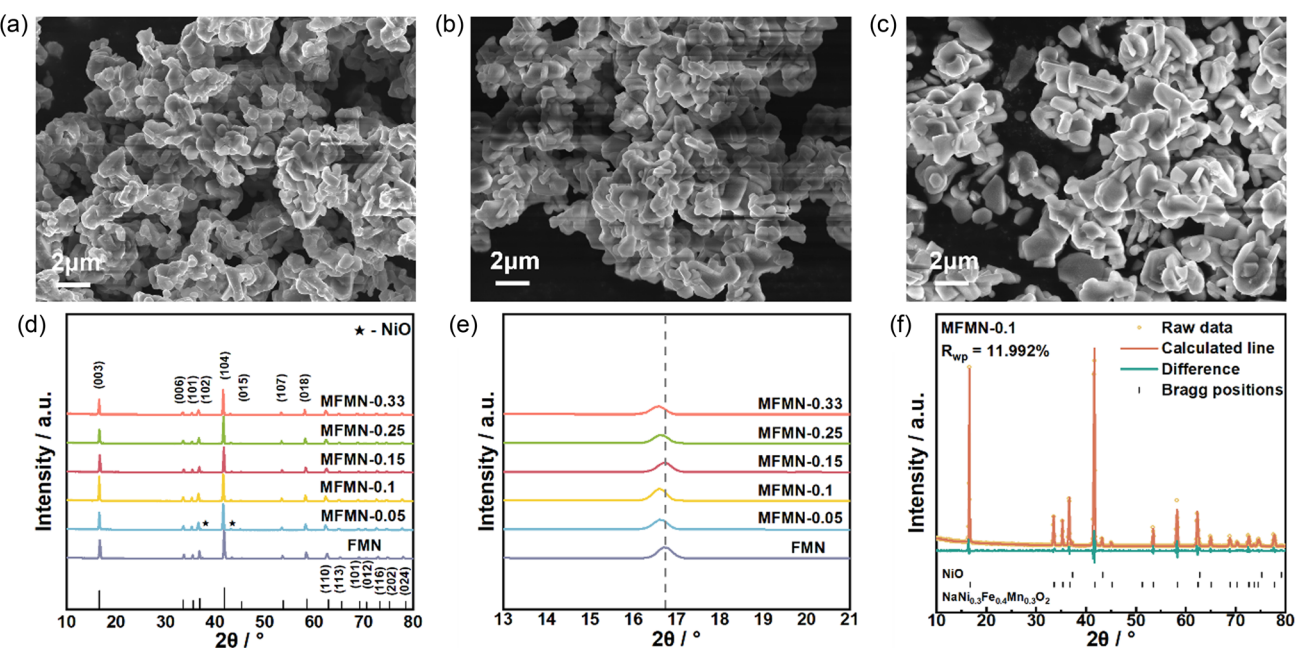


Figure 1. SEM images of a) FMN, b) MFMN-0.1, and c) MFMN-0.33. d) XRD patterns and e) the enlarged patterns near (003) peak of FMN, MFMN-0.05, MFMN-0.1, MFMN-0.15, MFMN-0.25, and MFMN-0.33. f) Refined XRD patterns of MFMN-0.1.

Information, displays the normalized Raman spectra of FMN and MFMN-0.1, in which three distinct peaks are observed at ≈ 353 , 501 , and 584 cm^{-1} , corresponding to the E_{2g} vibrational modes of Na-O bonds. Notably, all three peaks for MFMN-0.1 exhibit a blue shift toward higher wavenumbers. These systematic shifts toward higher wavenumbers clearly indicate the contraction of Na-O bonds, which aligns perfectly with our Rietveld refinement results showing slightly shortened Na-O bond lengths. Specifically, the unit cell volume exhibits a notable expansion, which can be primarily attributed to the larger atomic radius of Mg compared to Ni. Concurrently, the TM layer spacing increases while the Na-O bond length contracts, suggesting an enhanced electrostatic interaction between Na and O layers. Importantly, the TM-O bond length shows a distinct elongation, indicative of the stronger ionic character of the Mg-O bond relative to the Ni-O bond.^[15] These structural changes collectively indicate that Mg substitution could effectively modulate the local coordination environment and electronic structure of FMN, potentially influencing its electrochemical properties.

To elucidate the valence states of Ni, Mn, and Fe in both pristine FMN and MFMN-0.1, X-ray photoelectron spectroscopy (XPS) was employed (Figure S4, Supporting Information). The Ni $2p_{1/2}$ and $2p_{3/2}$ binding energy peaks, observed at ≈ 861.0 and 855.0 eV , respectively, are consistent with the oxidation state of Ni^{2+} in both samples (Figure S4a,b, Supporting Information). Analysis of the Mn XPS spectra reveals the area ratios of $\text{Mn}^{4+}:\text{Mn}^{3+}$ to be $80.9\%:19.1\%$ for FMN and $76.0\%:24.0\%$ for MFMN-0.1 (Figure S4c,d, Supporting Information), indicating that Mg substitution has a slight impact on the valence state of Mn. Similarly,

the Fe XPS spectra shows a change in the $\text{Fe}^{3+}:\text{Fe}^{2+}$ ratio from $71.8\%:29.2\%$ in FMN to $65.2\%:34.8\%$ in MFMN-0.1 (Figure S4e,f, Supporting Information), further supporting that Mg substitution does not significantly alter the valence states of these TMs in the FMN material.

Subsequently, the electrochemical performance of MFMN-x was evaluated through half-cell assembly followed by charge-discharge curve analysis. In comparison to FMN (Figure S5, Supporting Information), the MFMN-x cathodes exhibit much increased initial charge/discharge capacity following Mg substitution (Figure 2a). Notably, the discharge specific capacity increases from 88.2 mAh g^{-1} for FMN to 163.2 mAh g^{-1} for MFMN-0.1 before gradually decreasing to 96.2 mAh g^{-1} for MFMN-0.33, demonstrating a clear dependency on Mg substitution levels. The charge-discharge curves reveal two voltage plateaus at ≈ 3.2 and 4.1 V for MFMN-0.05, indicative of a charge compensation process provided by Ni^{2+} and an ORR induced by Mg^{2+} , respectively. Interestingly, depending on the increasing Mg contents, the initial charge curves undergo notable changes. Specifically, the plateau in the low-voltage region gradually shortens and eventually disappears, while the plateau in the high-voltage region extends. This transition results in a reduced ratio of low-to-high voltage plateau capacities depending on the increasing Mg substitution levels (Figure S6, Supporting Information), suggesting a mechanistic shift from Ni^{2+} -dominated charge compensation to ORR as the primary capacity contributor.^[16] The enhanced charge compensation provided by ORR and the reduced charge compensation from Ni^{2+} redox then lead to the initially increased, and then, decreased capacity for

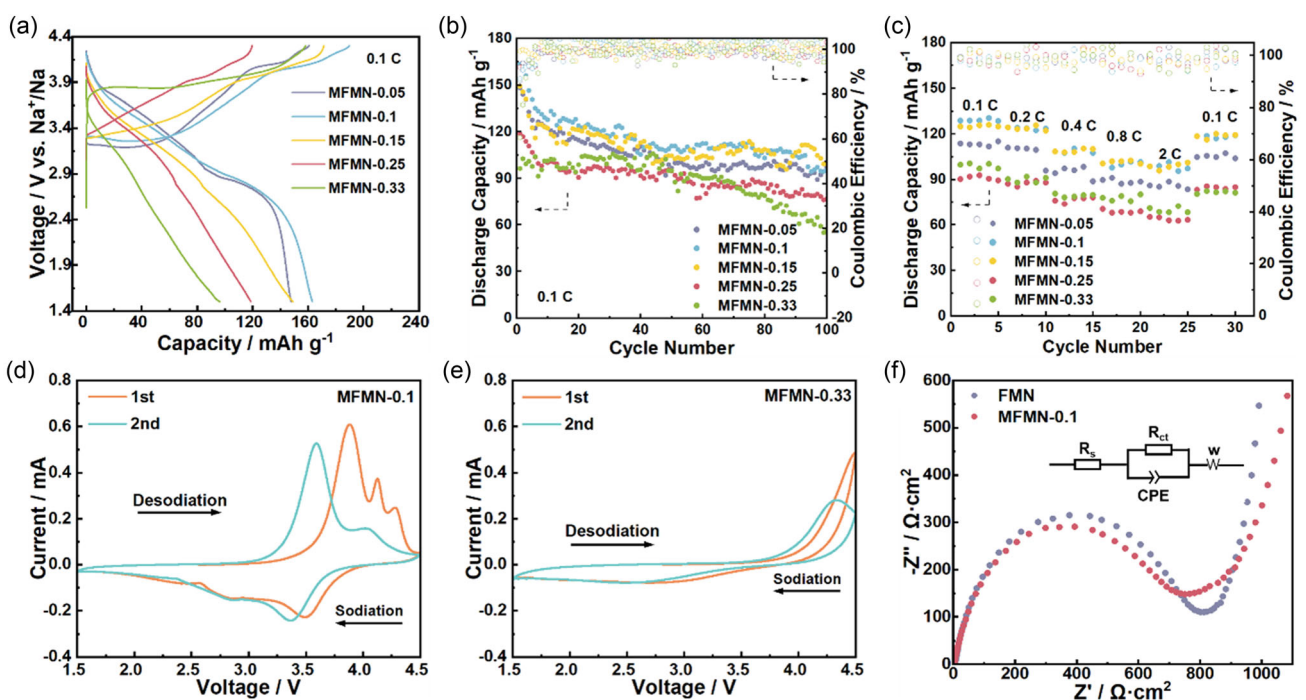


Figure 2. Electrochemical characterizations of MFMN-0.05, MFMN-0.1, MFMN-0.15, MFMN-0.25, and MFMN-0.33 cathodes. a) Initial charge-discharge curves and b) cycle performance at 0.1 C ($1 \text{ C} = 130 \text{ mAh g}^{-1}$). c) Rate performance. CV curves of d) MFMN-0.1 and e) MFMN-0.33. f) EIS curves of FMN and MFMN-0.1. R_s : ohmic resistance of the electrolyte and cell components, R_{ct} : charge transfer resistance at the electrode/electrolyte interface, and W : low-frequency Warburg impedance reflecting the solid-state diffusion limitations of Na^+ .

MFMN-x. Cycling performance tests further highlight the nonmonotonic relationship between Mg substitution level and capacity retention. Compared to the pristine FMN material, optimal Mg substitution enhances capacity retention to $\approx 65\%$, whereas excessive substitution (e.g., MFMN-0.33) degrades it to 58.2% (Figure 2b and S7, Supporting Information). This nonmonotonic trend is mirrored in rate capability tests: moderate Mg incorporation improves kinetics, while over-substitution induces increased irreversible ORR (Figure 2c). Collectively, these results establish a composition-performance correlation, wherein, partial Mg substitution enhances both the specific capacity and cycle stability of MFMN-x, while hyper-substitution leads to compromised performance. The observed “volcano-type” relationship underscores the critical balance between cationic substitution and structural integrity in designing high-performance electrodes.

To elucidate the underlying determinants of the enhanced electrochemical performance for Mg-substituted MFMN, cyclic voltammetry (CV) and electrochemical impedance spectroscopy (EIS) tests were performed. As shown in Figure 2d, the CV curves of MFMN-0.1 exhibit three oxidation peaks at ≈ 3.9 , 4.1, and 4.3 V during the initial cycle, paired with two reduction peaks at ≈ 3.5 and ≈ 2.9 V. These features are mechanistically assigned to the cation oxidation at ≈ 3.9 V and reduction at ≈ 2.9 V, while the peaks at ≈ 4.1 , ≈ 4.3 , and ≈ 3.5 V corresponding to ORR. Subsequent cycles demonstrate simplified phase transitions with diminished peak separation, reflecting low polarization and robust structural stability.^[17] Crucially, the attenuation of high-voltage peaks implies irreversible ORR activity, which correlates with capacity fade. In contrast, the CV curves of MFMN-0.33 (Figure 2e) exhibit fundamentally distinct electrochemical behavior compared to MFMN-0.1, with an oxygen oxidation peak emerging above 4.0 V during charging but no corresponding reduction peak during discharge. This observation confirms the limited participation of cationic species in charge compensation and the irreversible nature of oxygen redox in heavily substituted samples, ultimately leading to reduced capacity and cycle stability.^[18] Based on the discussion above, it can be concluded that Mg²⁺ substitution exerts dual effects on FMN cathode materials. While moderate substitution (e.g., MFMN-0.1) enhances structural stability, excessive substitution (e.g., MFMN-0.33) promotes irreversible oxygen redox activity. This dichotomy accounts for the observed “volcano-type” performance trend, where initial capacity enhancement is followed by progressive deterioration as Mg content increases.

To investigate the effects of Mg substitution on charge transfer properties of cathode materials, Nyquist plots were obtained (Figure 2f) and fitted using an equivalent circuit shown in the inset of Figure 2f. Both FMN and MFMN-0.1 exhibit similarly low Ohmic resistance (R_s , 5.63 and 4.10 $\Omega \text{ cm}^2$, respectively), consistent with their identical cell configurations. Notably, the marginally lower charge transfer resistance ($R_{ct} = 727.1 \Omega \text{ cm}^2$) observed for Mg-substituted MFMN-0.1 relative to unsubstituted FMN (777.0 $\Omega \text{ cm}^2$) demonstrates that Mg substitution systematically enhances interfacial charge transfer kinetics.^[19] The Warburg impedance component in the low-frequency regime confirms Na⁺ diffusion limitations and governed by

$$D_{\text{Na}^+} = \frac{R^2 T^2}{2 A^2 n^4 F^4 C^2 \sigma^2} \quad (1)$$

where R is gas constant, T is temperature, A is electrode surface area, n is the number of electrons transferred per molecule in the redox reaction, F is Faraday constant, C is the concentration of Na in the cathode material, and σ is Warburg factor. Furthermore, σ could be calculated according to

$$\sigma = R_s + R_{ct} + \sigma \omega^{-0.5} \quad (2)$$

where ω is angular frequency.^[20] The fitting data (Figure S8, Supporting Information) reveals that $\sigma_{\text{MFMN-0.1}} = 1.68 \sigma_{\text{FMN}}$ corresponding to a 65% reduction in Na⁺ diffusion coefficient ($D_{\text{MFMN-0.1}} = 0.35 D_{\text{FMN}}$) as calculated by Equation (1), indicating that Mg substitution introduces restricted Na⁺ diffusion.

To address the reversible ORR limitations in Mg-substituted cathode materials, Zn-substituted FMN (ZFMN-x; $x = 0.05, 0.1, 0.15, 0.22$) was synthesized via solid-state reaction and systematically investigated. The obtained ZFMN samples exhibit well-defined plate-like morphology as confirmed by SEM (Figure 3a–c) and TEM (Figure S9a, Supporting Information), with particle size increasing progressively from 1–2 μm (FMN) to $>10 \mu\text{m}$ (ZFMN-0.33) depending on the increasing Zn substitution levels, facilitating electrode processing by reducing particle agglomeration. For the representative ZFMN-0.15 sample, HRTEM and SAED verify its single-crystalline nature (Figure S9b,c, Supporting Information). Additionally, EDS mapping reveals uniform elemental distribution of all constituent species (Figure S10 and S11, Supporting Information), further validating the compositional homogeneity achieved through Zn substitution.

The XRD of FMN and ZFMN-x exhibit characteristic peaks fully consistent with the O3-type layered structure of $\text{NaNi}_{0.5}\text{Mn}_{0.5}\text{O}_2$, confirming that Zn substitution preserves the parent O3-phase framework without inducing structural phase transitions (Figure 3d). Interestingly, the diffraction intensity of NiO impurities in pristine FMN could be progressively diminished with increasing Zn substitution levels in ZFMN-0.05 and ZFMN-0.1, demonstrating Zn-mediated suppression of NiO phase formation. Concurrently, the emergence of ZnO secondary phases in ZFMN-0.15 and ZFMN-0.22 could be attributed to precursor-derived unreacted ZnO residues arising from Na/Ni stoichiometric imbalance during solid-state synthesis. The enlargement of XRD patterns, as shown in Figure 3e, reveals a shift of the (003) peak to lower angles depending on the increasing of Zn substitution levels, confirming successful Zn²⁺ incorporation into the crystal lattice and concomitant expansion of the TM interlayer spacing.^[21] One would note that the minimal Bragg angle is observed for ZFMN-0.15, corresponding to the maximal TM layer dilation, whereas the partial reversal of this trend in ZFMN-0.22 (Fe-free composition) suggests Zn-O bond contraction dominates in the absence of Fe³⁺-mediated lattice effects.^[22] In addition, Rietveld refinement of ZFMN-0.1 ($R_{wp} = 11.908\%$) demonstrates contracted lattice parameters (a, b, c) compared to FMN, which leads to smaller unit cell volume and a more compact, structurally stable layered framework induced by Zn substitution (Figure 3f and Table S3, Supporting Information). The normalized Raman spectrum of ZFMN-0.1 shows a noticeable blue shift of all three

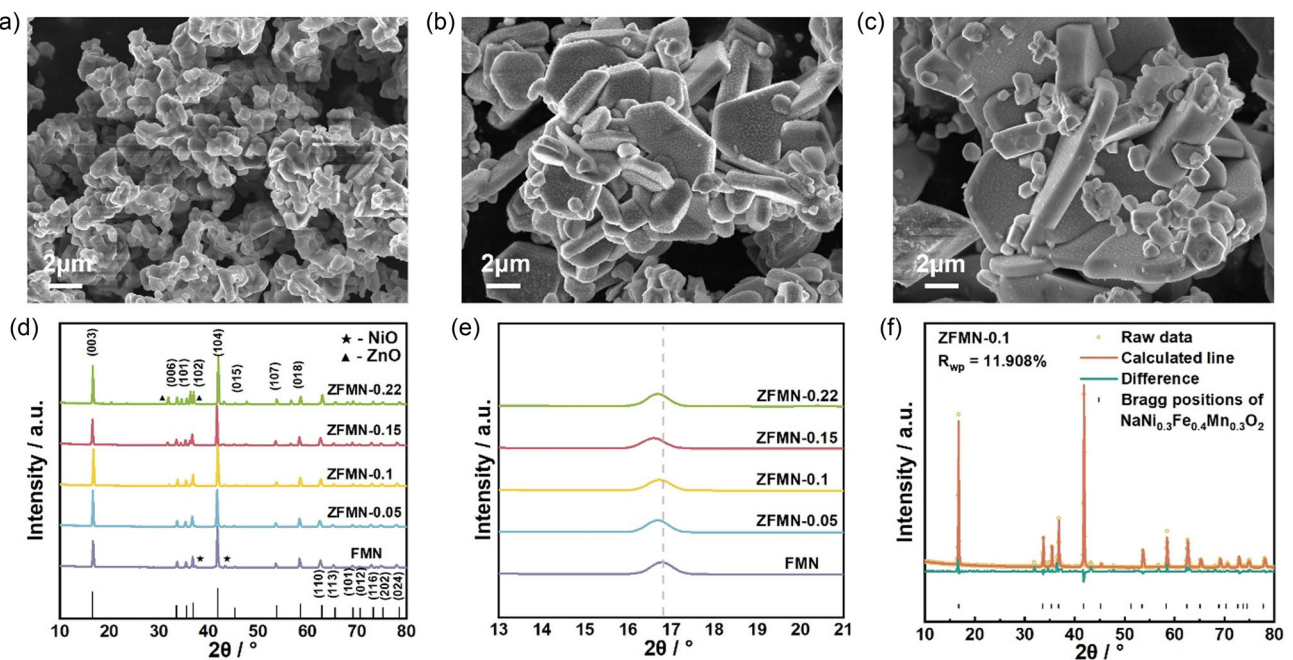


Figure 3. SEM images of a) FMN, b) ZFMN-0.15, and c) ZFMN-0.22. d) XRD patterns and e) the enlarged patterns near (003) peak of FMN, ZFMN-0.05, ZFMN-0.1, ZFMN-0.15, and ZFMN-0.22. f) Refined XRD patterns of ZFMN-0.1.

characteristic peaks, indicating a shortening of the Na-O bond lengths, which further confirms the reliability of the Rietveld refinement results (Figure S12, Supporting Information). This structural evolution optimizes Na⁺ diffusion channels through two synergistic mechanisms: 1) expanded TM layers and 2) shortened TM-O bonds, collectively contributing to enhanced electrochemical performance in Zn-substituted FMN-based cathode materials.

The electrochemical performance of ZFMN cathodes with varying Zn substitution levels was systematically investigated. In comparison to FMN (Figure S5, Supporting Information), Zn-substituted ZFMN-x cathodes exhibit significantly enhanced initial cycle charge/discharge capacities (Figure 4a). Notably, the discharge specific capacity is increased from 88.2 mAh g⁻¹ for FMN to 144.5 mAh g⁻¹ for ZFMN-0.15, and then, gradually decreased to 94.3 mAh g⁻¹ for ZFMN-0.22, correlating with increasing Zn substitution levels. During the first charge process, ZFMN-0.05, ZFMN-0.1, and ZFMN-0.15 display an abnormal voltage drop around 3.4 V, attributed to residual alkali on the surface.^[23] In contrast, ZFMN-0.22 exhibits multiple small plateaus, contrasting with the smoother curves observed in Fe-containing counterparts. This phenomenon originates from the critical role of Fe³⁺ in suppressing complex phase transitions during electrochemical cycling in Mn-based layered oxides. Complete Fe substitution by Zn triggers successive structural rearrangements, manifested as these small plateaus and contributing to the reduced initial discharge capacity of ZFMN-0.22 (Figure 4a). Cycle performance tests reveal that all Zn-substituted materials demonstrate comparable stability compared to FMN and MFMN analogs (Figure 4b), underscoring the universal efficacy of Zn substitution in mitigating structural degradation across substitution levels.^[24] Rate capability analysis (Figure 4c) reveals

comparable performance across all ZFMN variants, with ZFMN-0.15 achieving the highest reversible capacity under high current densities. This enhancement correlates with its optimized TM layer dilation and shortened TM-O bonds, which synergistically lower Na⁺ migration barriers while maintaining structural integrity. Collectively, these results demonstrate that partial Zn substitution (e.g., ZFMN-0.15) achieves an optimal balance between capacity enhancement and structural stability, positioning ZFMN cathodes as promising candidates for sodium-ion batteries.

The electrochemical performance enhancement through Zn substitution in ZFMN-x cathodes was further elucidated through CV and EIS analyses. Initial-cycle CV profiles of ZFMN-0.15 (Figure 4d) reveal two prominent oxidation peaks at 3.9 and 4.3 V, coupled with corresponding reduction peaks at 3.8 and 2.5 V, suggesting well-defined redox reactions involving TM cations. Subsequent cycles of ZFMN-0.15 maintain this electrochemical signature while developing additional oxidation features at 3.4 and 4.1 V, accompanied by stable reduction responses at 3.7 and 2.5 V. This electrochemical reversibility, particularly the persistent high-voltage redox couples, correlates with the enhanced cycling stability of ZFMN-0.15 compared to MFMN-0.1. In contrast, as shown in Figure 4e, CV curves of ZFMN-0.22 display multiple small redox peaks during both initial and subsequent cycles, mirroring the small plateaus observed in its charge-discharge curves (Figure 4a). These behaviors indicate successive phase transformations, a phenomenon suppressed in Fe³⁺-containing FMN due to its stabilizing effect on the host framework. The absence of Fe³⁺ in heavily substituted ZFMN-0.22 destabilizes the host structure, leading to electrochemical performance degradation.^[25]

EIS analysis of ZFMN-0.15 and FMN (Figure 4f) reveals the kinetic enhancement mechanism through Zn substitution.

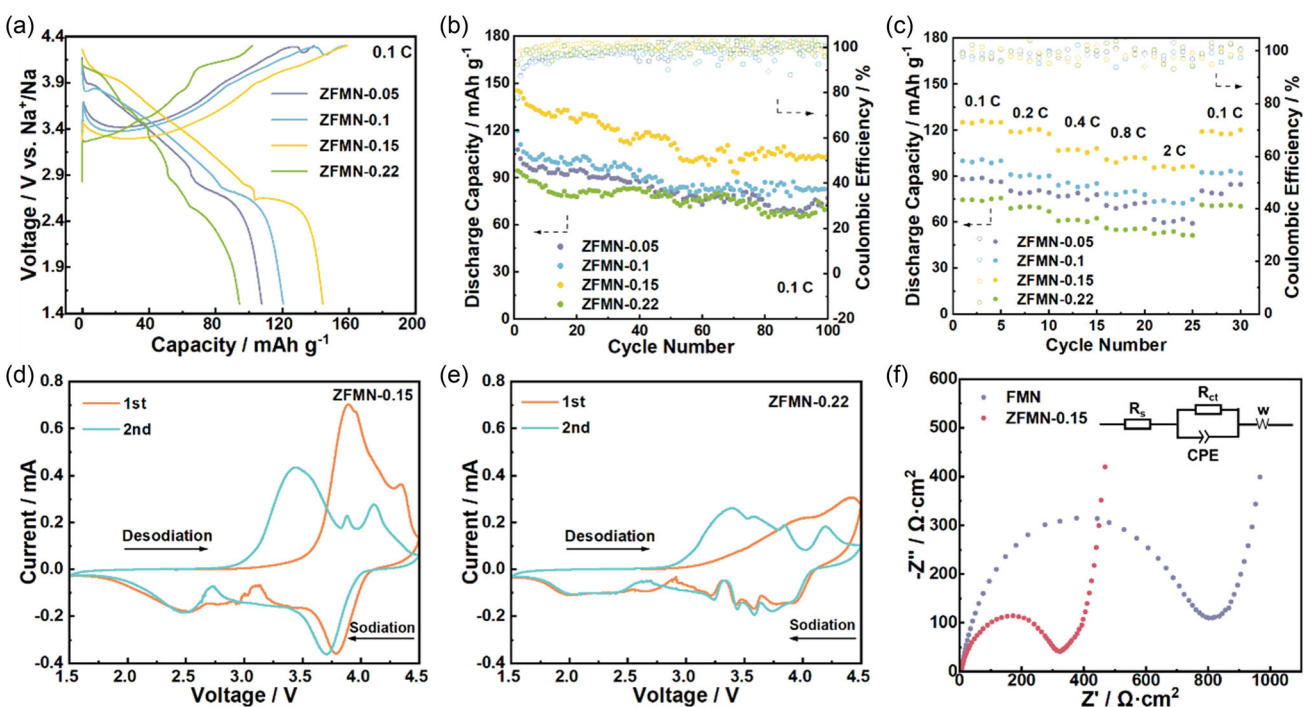


Figure 4. Electrochemical characterizations of ZFMN-0.05, ZFMN-0.1, ZFMN-0.15, and ZFMN-0.22 cathodes. a) Initial charge–discharge curves and b) cycle performance at 0.1 C. c) Rate performance. CV curves of d) ZFMN-0.15 and e) ZFMN-0.22. f) EIS curves of FMN and ZFMN-0.15, R_s : ohmic resistance of the electrolyte and cell components, R_{ct} : charge transfer resistance at the electrode/electrolyte interface, and W: low-frequency Warburg impedance reflecting the solid-state diffusion limitations of Na^+ .

While both materials exhibit similar Ohmic resistance (R_s), the charge transfer resistance (R_{ct}) of ZFMN-0.15 is significantly lower than that of FMN, indicating significantly improved electronic conductivity from Zn^{2+} -induced charge redistribution, which facilitates electron transfer at the electrode–electrolyte interface. Warburg analysis further demonstrates that ZFMN-0.15 achieves a reduced Warburg constant ($\sigma_{\text{ZFMN-0.15}} = 0.65\sigma_{\text{FMN}}$), corresponding to a 2.37-fold increase in Na^+ diffusion coefficient (Figure S13, Supporting Information). These improvements stem from Zn substitution induced dual effects: optimizing charge transfer through electronic structure modulation and facilitating ionic diffusion via expanded interlayer spacing. The apparent inconsistency between covalent Zn-O bonding and the observed enhancement in Na^+ diffusion dynamics can be resolved by considering three synergistic effects. First, the strong covalent Zn-O bonds provide structural stability by preventing layer sliding and collapse during cycling, thereby maintaining continuous Na^+ diffusion pathways. Second, the high charge density of Zn^{2+} ions locally weakens Na-O bonding strength, which effectively reduces the Na^+ migration energy barrier by optimizing the interlayer spacing and local coordination environment. Third, Zn substitution minimizes parasitic side reactions at the electrode/electrolyte interface, reducing the formation of resistive surface layers. These combined effects, including structural stabilization, local bonding modification, and interface protection, collectively contribute to both the reduced charge transfer resistance (R_{ct}) observed in EIS measurements and the improved Na^+ diffusion kinetics, demonstrating that covalent Zn-O bonding and enhanced ionic transport are fundamentally interconnected.

To leverage the benefits of Mg and Zn substitution, the synergistic effects of Mg-Zn cosubstitution were systematically investigated in the designed $\text{NaMg}_{0.1}\text{Zn}_{0.15}\text{Fe}_{0.11}\text{Mn}_{0.4}\text{Ni}_{0.23}\text{O}_2$ (MZFMN). The cosubstituted material exhibits well-defined plate-like morphology (2–4 μm) and homogeneous elemental distribution, as confirmed by SEM, TEM, and scanning TEM-EDS analysis (Figure 5a–f). HRTEM further reveals the single-crystal nature of MZFMN particles with well-ordered TM layers, demonstrating both successful synthesis via solid-state method and good crystallinity (Figure 5g,h). Structural characterizations show that the cosubstituted material maintains the O3-type layered structure while exhibiting increased expansion in TM layer spacing compared to FMN, MFMN-0.1, and ZFMN-0.15 (Figure S14a,b, Supporting Information). This lattice expansion, attributed to the combined effects of Zn^{2+} and Mg^{2+} , is expected to facilitate enhanced Na^+ diffusion kinetics.

Then, the electrochemical performance of Mg-Zn cosubstituted MZFMN was investigated through galvanostatic charge–discharge tests. As shown in Figure 6a, MZFMN demonstrates the most stable electrochemical behavior among the three modified materials (MFMN-0.1, ZFMN-0.15, and MZFMN), as evidenced by its smooth voltage profile with minimal plateaus, indicative of its superior electrochemical stability. While MFMN-0.1 shows the highest initial discharge capacity (163.2 mAh g^{-1}), the cosubstituted MZFMN material achieves an optimal balance between initial capacity (154.5 mAh g^{-1}) and cycling stability, maintaining 78.0% capacity retention after 100 cycles compared to 64.3% and 71.6% for MFMN-0.1 and ZFMN-0.15, respectively (Figure 6b). This enhanced cyclability can be attributed to the

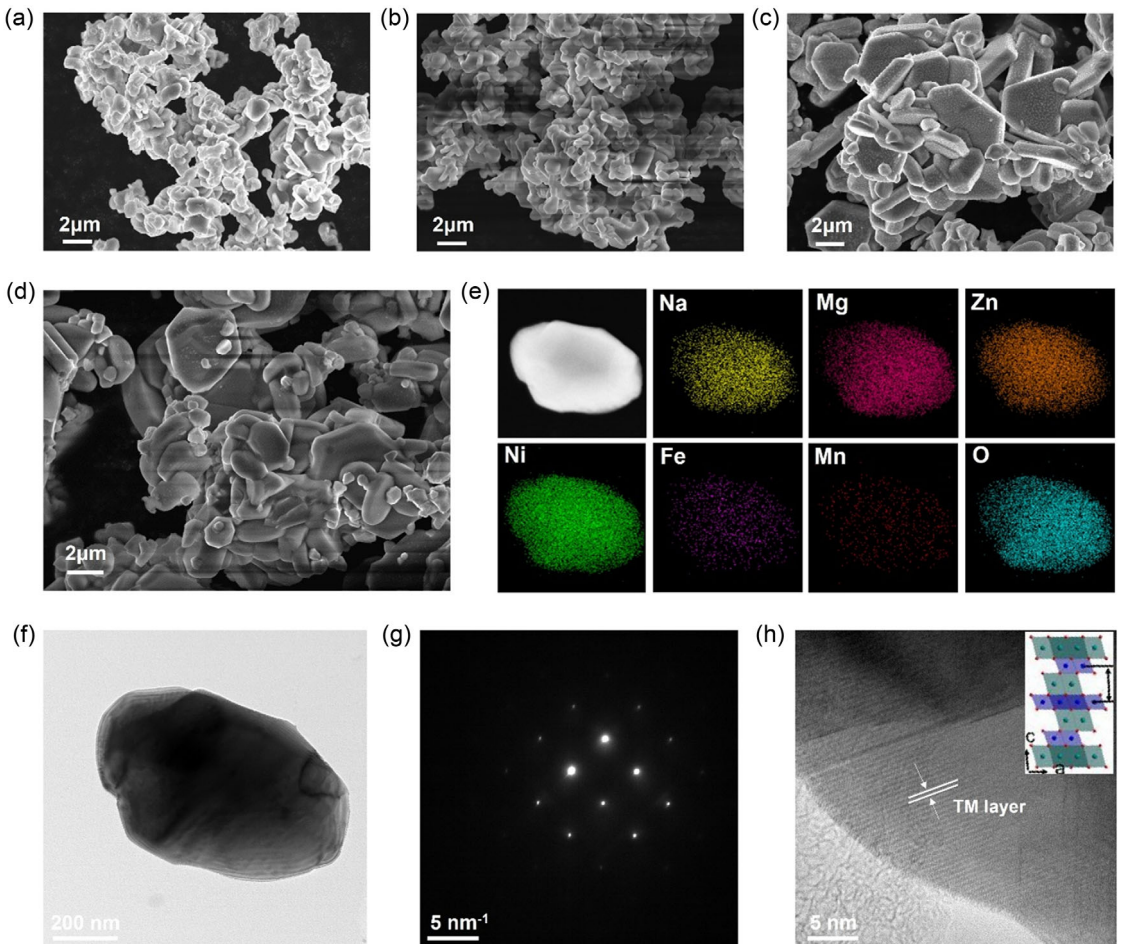


Figure 5. SEM images of a) FMN, b) MFMN-0.1, c) ZFMN-0.15, and d) MZFMN. e) STEM image and EDS mapping, f) TEM image, g) SAED pattern, and h) HRTEM image of MZFMN.

synergistic stabilization effects of Mg^{2+} and Zn^{2+} cosubstitution, which effectively suppress irreversible phase transitions through entropy-driven structural stabilization. To further investigate the synergistic effect of Mg/Zn dual-site substitution and high-entropy engineering on structural stability, XRD and SEM characterizations were conducted on FMN and MZFMN electrodes after long-term cycling. The XRD patterns (Figure S15, Supporting Information) show that the characteristic peak near 45° for pristine FMN significantly weakens or even disappears after cycling, indicating irreversible lattice distortion or cation disordering in its layered structure. In contrast, MZFMN retains well-defined diffraction peaks after cycling, confirming that the high-entropy configuration effectively suppresses detrimental phase transitions. Moreover, SEM analysis further reveals the differences in structural stability. Pronounced cracks are observed on the surface of cycled FMN particles (Figure S16a,b, Supporting Information), which result from anisotropic stress accumulation during repeated charge–discharge processes. In comparison, the MZFMN particles (Figure S16c,d, Supporting Information) maintain relatively well plate-like morphology with intact particle boundaries. This stark contrast demonstrates how the synergistic combination of Zn^{2+} induced covalent bonding and entropy-enhanced lattice toughness effectively dissipates mechanical

stress. Furthermore, rate capability tests demonstrate the superior high rate performance of MZFMN, with 81.3% capacity retention at 2 C relative to 0.1 C (Figure 6c), confirming the advantages of the dual-cation substitution strategy in improving kinetic property of the cathode material. These results collectively highlight the effectiveness of Mg-Zn cosubstitution in developing high-performance sodium-ion battery cathodes with balanced capacity, cycling stability, and rate capability.

Electrochemical characterization could provide critical insights into the reaction mechanisms and kinetic properties of the modified cathode materials. The CV curves of MZFMN (Figure 6d) reveal a distinct oxidation peak at ≈ 3.8 and 4.1 V during the first charge–discharge cycle, assigning to the sequential oxidation of TM ions. A corresponding reduction peak appears at ≈ 3.3 V during discharge, confirming the reversibility of electrochemical reactions. In the second cycle, the oxidation peak shifts slightly to ≈ 3.6 V while the reduction peak remains unchanged, suggesting the formation of a stabilized electrochemical interface after initial activation. This simplified CV behavior, characterized by minimal peak shifts and maintained peak symmetry, strongly supports the proposed entropy-stabilization mechanism that effectively suppresses complex phase transitions during cycling.

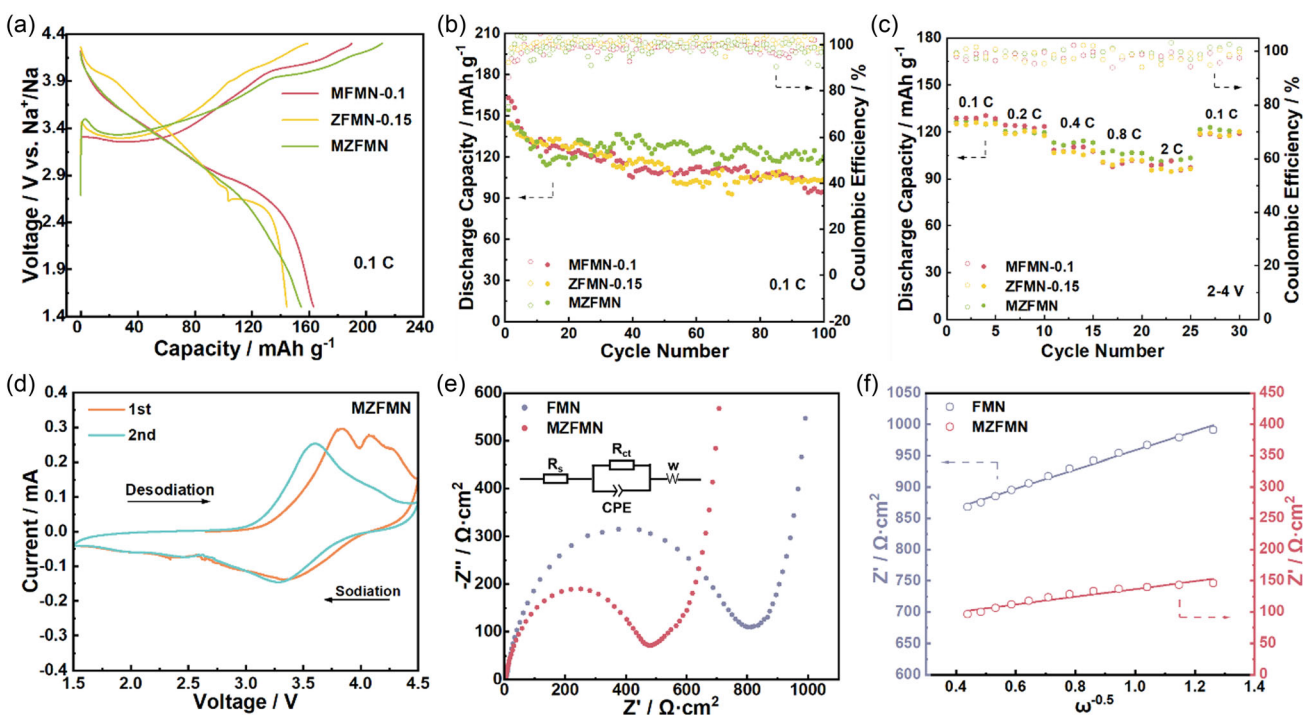


Figure 6. Electrochemical characterizations of MFMN-0.1, ZFMN-0.15, and MZFMN cathodes. a) Initial charge–discharge curves and b) cycle performance at 0.1 C. c) Rate performance. d) CV curves of MZFMN. e) EIS curves, R_s : ohmic resistance of the electrolyte and cell components, R_{ct} : charge transfer resistance at the electrode/electrolyte interface, and W : low-frequency Warburg impedance reflecting the solid-state diffusion limitations of Na^+ . f) Fitting results of Z' and $\omega^{-0.5}$ of FMN and MZFMN.

Additionally, EIS measurements reveal that while both FMN and MZFMN exhibit similar R_s , the cosubstituted material shows significantly reduced R_{ct} , indicating enhanced interfacial charge transfer kinetics (Figure 6e). This improvement can be attributed to the synergistic effects of Mg–Zn cosubstitution, which optimizes both electronic conductivity and ionic transport properties. Further analysis of Na^+ diffusion kinetics (Figure 6f) demonstrates that the cosubstitution strategy could successfully balance the opposing effects of individual dopants (Table S4, Supporting Information). While Mg substitution tends to decrease the Na^+ diffusion coefficient due to its strong oxygen affinity, Zn substitution facilitates ionic transport through its electronic structure modification, ultimately resulting in a net improvement in the Na^+ diffusion coefficient for MZFMN. To evaluate the electrochemical performance of this dual-substitution cathode material, we have conducted a systematic comparison between our approach and state-of-the-art stabilization methods for layered oxide cathodes, as comprehensively summarized in Table S5, Supporting Information. The comparative analysis reveals several key advantages of our dual-substitution strategy: MFMN-0.1 achieves a remarkable specific capacity of 163.2 mAh g⁻¹ at 0.5 C, outperforming most reported binary (typically 120–140 mAh g⁻¹) and ternary (140–160 mAh g⁻¹) systems, while the MZFMN sample demonstrates superior trade-off characteristics with 154.5 mAh g⁻¹ capacity and 78.0% retention after 100 cycles, surpassing many quaternary systems in cycling stability while maintaining competitive capacity. Notably, both materials exhibit stable voltage profiles throughout cycling, contrasting with the severe voltage decay observed in conventional

single-substitution approaches. This comprehensive comparison establishes that our dual-substitution strategy uniquely combines high capacity with excellent cycling stability, addressing the common trade-off between these parameters in existing stabilization methods, thereby validating our methodology's novelty and practical advantages for next-generation sodium-ion battery cathodes.

3. Conclusion

In this study, a dual-site substitution strategy combined with high-entropy engineering was presented to synergistically address structural instability and irreversible oxygen redox in Fe–Mn–Ni layered oxides for sodium-ion battery cathodes. Through systematic optimization, the designed $\text{NaMg}_{0.1}\text{Zn}_{0.15}\text{Fe}_{0.11}\text{Mn}_{0.4}\text{Ni}_{0.23}\text{O}_2$ (MZFMN) cathode demonstrates exceptional electrochemical performance, delivering a high initial discharge capacity of 154.5 mAh g⁻¹ while maintaining 78% capacity retention after 100 cycles, which shows a significant improvement over conventional single-substituted counterparts. Comprehensive characterizations reveals that this performance enhancement originates from the complementary functionalities of Mg and Zn cosubstitution, with Mg activating reversible oxygen redox to boost capacity, while Zn stabilizing the layered framework through strong covalent bonding, suppressing detrimental phase transitions. Furthermore, the high-entropy configuration induced by multication substitution enhances structural stability through lattice disorder and configurational entropy effects, collectively

mitigating irreversible structural degradation during prolonged cycling. This synergistic strategy decouples the traditional trade-off between capacity and stability, offering a versatile design paradigm for advanced cathode materials. Our findings underscore the potential of entropy-driven engineering combined with targeted cation substitution to unlock high-performance, durable SIBs for scalable energy storage applications.

Acknowledgements

The authors thank the National Natural Science Foundation of China (Grant No. 52225606) and the Hunan Desai Battery Co., Ltd technology development project (Grant No. 32111000001273).

Conflict of Interest

The authors declare no conflict of interest.

Data Availability Statement

The data that support the findings of this study are available from the corresponding author upon reasonable request.

Keywords: dual-site substitutions · Fe–Mn–Ni based layered oxides · high-entropy engineering · sodium-ion battery

- [1] J.-Y. Hwang, S.-T. Myung, Y.-K. Sun, *Chem. Soc. Rev.* **2017**, *46*, 3529.
- [2] T. P. Nguyen, I. T. Kim, *Materials* **2023**, *16*, 6869.
- [3] a) C. Deng, E. Gabriel, P. Skinner, S. Lee, P. Barnes, C. Ma, J. Gim, M. L. Lau, E. Lee, H. Xiong, *ACS Appl. Mater. Interfaces* **2020**, *12*, 51397; b) S. Zhao, Q. Shi, W. Feng, Y. Liu, X. Yang, X. Zou, X. Lu, Y. Zhao, *Carbon Neutrality* **2023**, *2*, 13.
- [4] a) N. Li, K. Wu, Y. L. Lee, D. Rongbin, X. Deng, Z. Hu, X. Xiao, *Nanoscale* **2020**, *12*, 16831; b) B. Zhang, Y. Zhao, M. Li, Q. Wang, X. Wang, L. Cheng, L. Ming, X. Ou, X. Wang, *ACS Appl. Mater. Interfaces* **2023**, *15*, 50994; c) X. Li, D. Wu, Y.-N. Zhou, L. Liu, X.-Q. Yang, G. Ceder, *Electrochem. Commun.* **2014**, *49*, 51; d) T. Y. Yu, H. H. Ryu, G. Han, Y. K. Sun, *Adv. Energy Mater.* **2020**, *10*, 2001609.
- [5] K. Dai, J. Wu, Z. Zhuo, Q. Li, S. Sallis, J. Mao, G. Ai, C. Sun, Z. Li, W. E. Gent, W. C. Chueh, Y. Chuang, R. Zeng, Z. Shen, F. Pan, S. Yan, L. F. J. Piper, Z. Hussain, G. Liu, W. Yang, *Joule* **2019**, *3*, 518.
- [6] Y. Niu, Z. Hu, B. Zhang, D. Xiao, H. Mao, L. Zhou, F. Ding, Y. Liu, Y. Yang, J. Xu, W. Yin, N. Zhang, Z. Li, X. Yu, H. Hu, Y. Lu, X. Rong, J. Li, Y. S. Hu, *Adv. Energy Mater.* **2023**, *13*, 2300746.
- [7] M. Liu, J. Zhang, Y. Peng, S. Guan, *Dalton Trans.* **2024**, *53*, 8940.
- [8] J. Billaud, G. Singh, A. R. Armstrong, E. Gonzalo, V. Roddatis, M. Armand, T. Rojo, P. G. Bruce, *Energy Environ. Sci.* **2014**, *7*, 1387.
- [9] C. Shi, L. Wang, X. A. Chen, J. Li, S. Wang, J. Wang, H. Jin, *Nanoscale Horiz.* **2022**, *7*, 338.
- [10] a) M. Weber, J. K. Mayer, A. Kwade, *Energy Technol.* **2023**, *11*, 2201299; b) M.-T. F. Rodrigues, S. E. Trask, I. A. Shkrob, D. P. Abraham, *J. Power Sources* **2018**, *395*, 289.
- [11] a) X. Xu, H. Huo, J. Jian, L. Wang, H. Zhu, S. Xu, X. He, G. Yin, C. Du, X. Sun, *Adv. Energy Mater.* **2019**, *9*, 1803693; b) J. Wang, X. Lu, Y. Zhang, J. Zhou, J. Wang, S. Xu, *J. Energy Chem.* **2022**, *65*, 681.
- [12] S. Gao, Z. Zhu, H. Fang, K. Feng, J. Zhong, M. Hou, Y. Guo, F. Li, W. Zhang, Z. Ma, F. Li, *Adv. Mater.* **2024**, *36*, 2311523.
- [13] a) Y. Yu, J. Zhang, R. Gao, D. Wong, K. An, L. Zheng, N. Zhang, C. Schulz, X. Liu, *Energy Environ. Sci.* **2023**, *16*, 584; b) K. Zhang, Z. Xu, G. Li, R. J. Luo, C. Ma, Y. Wang, Y. N. Zhou, Y. Xia, *Adv. Energy Mater.* **2023**, *13*, 2302793; c) L. Feng, Y. Xia, J. Guo, H. Liu, Y. Hao, Z. Tian, X. Xiao, L. Feng, C. Sun, S. Qi, K. Li, Y. Li, Y. Jiang, *Chem. Eng. J.* **2024**, *496*, 154298.
- [14] M. Li, H. Zhuo, J. Lei, Y. Guo, Y. Yuan, K. Wang, Z. Liao, W. Xia, D. Geng, X. Sun, J. Hu, B. Xiao, *Nat. Commun.* **2025**, *16*, 2010.
- [15] K. Sada, S. Kmiec, A. Manthiram, *Angew. Chem., Int. Ed.* **2024**, *63*, e202403865.
- [16] a) Y. Liu, S. Li, Z.-Y. Gu, Y.-L. Heng, H.-Y. Lü, J.-L. Yang, M. Du, X.-T. Wang, J.-Z. Guo, F. Dong, K. Li, X.-L. Wu, *Energy Storage Mater.* **2024**, *68*, 103319; b) Q. Liu, W. Zheng, X. Su, X. Zhang, N. Han, Z. Wang, J. Luo, Z. Lu, J. Fransaer, *Chem. Eng. J.* **2023**, *452*, 139337; c) Q. Zhou, Y. Xin, Y. Wang, Z. Wang, X. Ding, C. Sun, L. Liu, Q. Wang, F. Wu, E. Sheha, H. Gao, *Energy Storage Mater.* **2025**, *76*, 104138.
- [17] a) K. Zhang, B. Li, Y. Zuo, J. Song, H. Shang, F. Ning, D. Xia, *Electrochem. Energy Rev.* **2019**, *2*, 606; b) S. Ahmed, K. Volz, *Matter* **2023**, *6*, 1682.
- [18] Y.-J. Guo, P.-F. Wang, Y.-B. Niu, X.-D. Zhang, Q. Li, X. Yu, M. Fan, W.-P. Chen, Y. Yu, X. Liu, Q. Meng, S. Xin, Y.-X. Yin, Y.-G. Guo, *Nat. Commun.* **2021**, *12*, 5267.
- [19] C. Zhan, W. Liu, M. Hu, Q. Liang, X. Yu, Y. Shen, R. Lv, F. Kang, Z.-H. Huang, *NPG Asia Mater.* **2018**, *10*, 775.
- [20] N. Böckenfeld, A. Balducci, *J. Solid State Electrochem.* **2013**, *18*, 959.
- [21] W. Zheng, Q. Liu, Z. Wang, Z. Yi, Y. Li, L. Cao, K. Zhang, Z. Lu, *J. Power Sources* **2019**, *439*, 227086.
- [22] K. Shimokawa, T. Atsumi, M. Harada, R. E. Ward, M. Nakayama, Y. Kumagai, F. Oba, N. L. Okamoto, K. Kanamura, T. Ichitsubo, *J. Mater. Chem. A* **2019**, *7*, 12225.
- [23] L. Feng, J. Guo, C. Sun, X. Xiao, L. Feng, Y. Hao, G. Sun, Z. Tian, T. Li, Y. Li, Y. Jiang, *Small* **2024**, *20*, 2403084.
- [24] a) W. Ling, C. Nie, X. Wu, X.-X. Zeng, F. Mo, Q. Ma, Z. Lu, G. Luo, *ACS Nano* **2024**, *18*, 5003; b) W. Ling, F. Mo, X. Wu, X.-X. Zeng, J. Xiong, Y. Huang, *Nat. Commun.* **2025**, *16*, 152324; c) G.-Y. Yin, H.-R. Wang, W. Ling, X. Wu, J. Dai, X.-X. Zeng, *Angew. Chem., Int. Ed.* **2025**, *64*, e202423244.
- [25] a) Y. Qiu, Q. Shi, X. Yu, Y. Liu, Y. Liu, W. Feng, J. Wang, Y. Zhao, *Chem. Eng. Sci.* **2024**, *300*, 120671; b) S. Zhao, F. Ning, X. Yu, B. Guo, J. Huang, Q. Shi, S. Wu, W. Feng, Y. Zhao, *Angew. Chem., Int. Ed.* **2024**, *64*, e202416290.

Manuscript received: May 29, 2025

Revised manuscript received: July 4, 2025

Version of record online: